







## Probing the local thermal conductivity of single- and multidomain ferroelastic variants of BiFeO<sub>3</sub> by Raman thermometry

Ayberk Özden <sup>1,\*</sup>, Felix Drechsler <sup>1</sup>, Jens Kortus <sup>1</sup>, Marin Alexe <sup>2</sup> and Cameliu Himcinschi <sup>1</sup>

<sup>1</sup>*Institut für Theoretische Physik, TU Bergakademie Freiberg, Leipziger Str. 23, 09599 Freiberg, Germany*

<sup>2</sup>*Department of Physics, University of Warwick, Coventry CV4 7AL, United Kingdom*

 (Received 28 August 2023; revised 9 November 2023; accepted 13 December 2023; published 24 January 2024)

In this work, the optothermal Raman technique was used to measure the local thermal conductivity of macro/single ferroelastic domains of bulk BiFeO<sub>3</sub> (BFO) crystal and multidomain epitaxially grown thin film (~180 nm) on DyScO<sub>3</sub> (DSO) substrate. Domain walls (DWs) were found to act as effective phonon scatterers, reducing the thermal conductivity at room temperature from 2.17 to 1.16 W/mK and from 9.89 to 3.20 W/mK at 150 K. The results indicate that BFO is a promising candidate for bidirectional thermal conductivity tuning and switchable nonlinear thermal components if the DW density can be modulated by an externally applied field.

DOI: [10.1103/PhysRevMaterials.8.014407](https://doi.org/10.1103/PhysRevMaterials.8.014407)

### I. INTRODUCTION

The control of phonon propagation in materials is of great importance for thermal management, energy harvesting, and switchable nonlinear thermal components [1–3]. The thermal conductivity of a material can be controlled using engineered phonon scattering centers, such as point defects and interfaces (e.g., grain boundaries, precipitates, and heterostructures) through various processing techniques and once set, cannot be subsequently changed at a given temperature [4,5]. These approaches have been widely used to improve the performance of thermoelectric materials by hindering phonon propagation [6]. However, further tuning of the heat flow with the help of an external field seems difficult due to the lack of mass and charge of lattice vibrations [7]. Therefore, new material systems are needed to dynamically control the thermal conductivity of a material at a fixed temperature through electric, magnetic, or strain fields. Ferroelectric and ferroelastic materials have been proposed to fulfill this requirement thanks to the configurable domain structure and domain walls (DWs) acting as phonon scattering planes for the incident phonons [7–10].

Atomistic transport calculations have predicted that DWs strongly scatter transverse phonons and transmit longitudinally polarized modes [7]. Moreover, it has been theoretically revealed that DWs possess a thermal boundary resistance (TBR) and overall TBR strongly depends on the DW density [11]. In line with the theoretical predictions, early studies have shown that the thermal conductivity of BaTiO<sub>3</sub> and KH<sub>2</sub>PO<sub>4</sub> bulk perovskites can be dynamically modulated as a function of DW density, which depends on the applied electric field [12,13]. However, the observed effect for these bulk systems was limited for low temperatures (30 K) due to the longer mean free path of phonons and larger DW separation. Successful decrease of DW spacing have yielded significant room temperature reversible tuning of thermal conductivity for polycrystalline ferroelectric thin

films of Pb(Zr<sub>0.3</sub>Ti<sub>0.7</sub>)O<sub>3</sub> (11%), suspended membranes of Pb(Zr<sub>0.3</sub>Ti<sub>0.7</sub>)O<sub>3</sub> (13%), and epitaxial-strain-engineered thin films of PbTiO<sub>3</sub> (61%) [14–16]. Multiferroics, therefore, opens up the potential for bidirectional thermal conductivity tuning and thermal switches.

BiFeO<sub>3</sub> (BFO) is another multiferroic material that offers simultaneous antiferromagnetic ( $T_N \approx 643$  K) and ferroelectric ( $T_C \approx 1083$  K) order at room temperature and is of significant interest in multifunctional, low power consumption and eco-friendly devices [17–19]. Moreover, there is considerable potential to engineer the ferroic domain structure of BFO through various strategies such as chemical modification, electrostatic boundary control, strain, and substrate engineering [20]. Furthermore, BFO possesses three polymorphs: rhombohedral (bulk), R- and T-like (reported for epitaxially grown thin films with monoclinic distortion), and one metamorphic phase transition between the R and T phases with external stimuli [21,22]. Therefore, BFO stands as an ideal candidate for bidirectional control of thermal conductivity. Moreover, thermal conductivity information is important for evaluating the performance of other applications, such as the recently emerging BFO solar cells [23].

A review of studies on the manipulation of the thermal conductivity of BFO at room temperature reveals that more work is needed. For example, Ning *et al.* reported *in situ* thermal conductivity variation with external electric field, while Hopkins *et al.* showed thermal conductivity of different domain wall variants (one to four) [9,24]. Ning *et al.* have found a negligible dependence of thermal conductivity on the domain wall density varied by the applied voltage for the 30-nm-thick epitaxial films of R- and T-like phases. However, they did not exclude the possibility of DWs being parallel to the heat flow due to the small film thickness. They also reported a strong thermal conductivity difference between R- (1.29–1.32 W/mK) and T-like BFO (0.82–0.84 W/mK) films [24]. On the other hand, Hopkins *et al.* showed a strong domain wall dependence of thermal conductivity and thermal boundary conductance for 30-nm-thick epitaxially grown thin films of one (single domain, ~2.15 W/mK), two

\*ao94huqi@mailserver.tu-freiberg.de

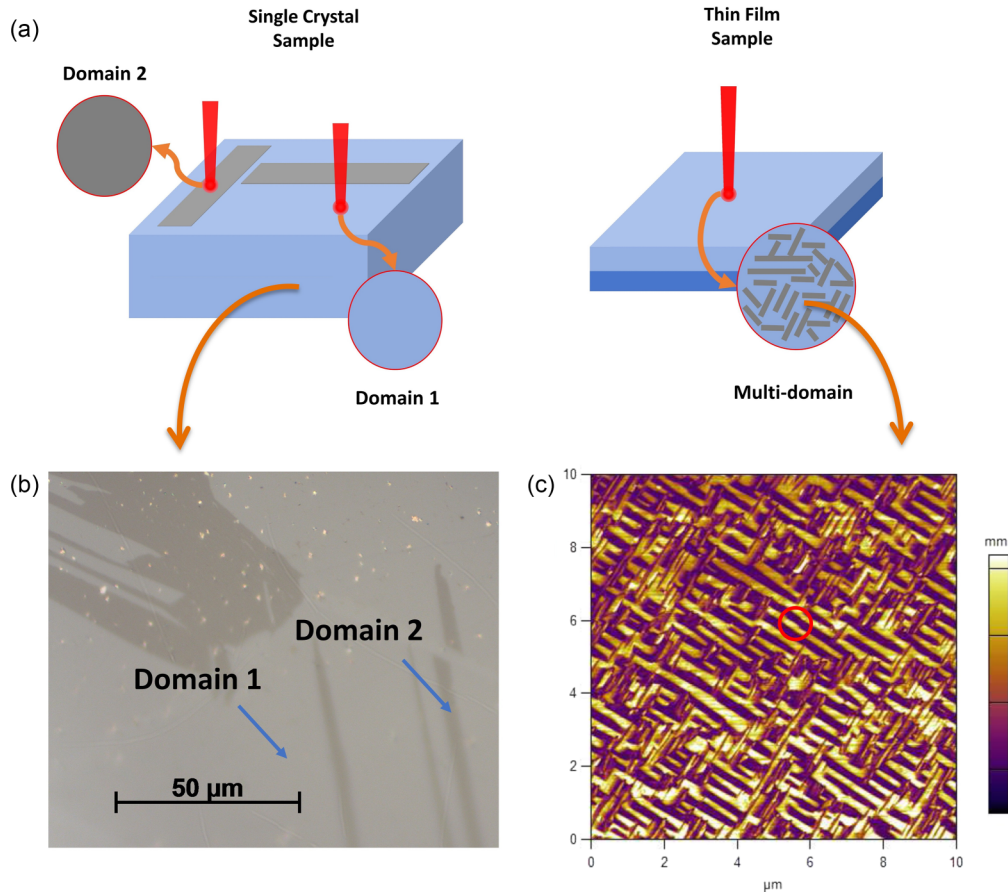


FIG. 1. (a) Schematic overview of experimental design, (b) POM image of bulk BFO crystal with marked macro (domain 1) and stripelike (domain 2) domains, and (c) PFM image of epitaxial BFO thin film on DSO substrate. Red circle represents arbitrarily positioned and scaled laser spot size ( $\sim 860$  nm) covering four DWs.

( $\sim 1.67$  W/mK), and four domain variants ( $\sim 1.50$  W/mK) at room temperature [9]. Therefore, for the specific case of BFO the effect of DWs on thermal conductivity needs to be further explored.

Here, the optothermal Raman method (OTR) was used to locally investigate the thermal conductivities of different BFO systems in terms of single- and multidomain variants within a diffraction-limited spatial resolution. OTR is a noncontact, all-optical method that does not require additional transducer metallic layers as used for frequency-domain thermoreflectance (FDTR)/time-domain thermoreflectance (TDTR), thus probing directly the materials properties [25]. The thermal conductivity of a bulk BFO crystal having macro/single-domain structure was compared to a relatively thick ( $\sim 180$  nm) epitaxially grown film with an average domain separation of  $\sim 200$  nm. Thus, this OTR study allows a direct reveal of the influence of DWs on global BFO thermal conductivity.

## II. EXPERIMENTAL DETAILS AND SAMPLES

Considering the limitations of the bulk OTR model [26,27], two samples with markedly different domain sizes were selected. For the bulk single-crystal BFO, as schematically shown in Fig. 1(a), a careful positioning of the laser spot with  $\mu$ -Raman technique ensures probing of a single domain without any DW contribution. For the thin-film sample the spot

size guarantees probing of at least two DWs. Therefore, the local thermal conductivity information from OTR can provide a solution to discriminate a DW effect.

An oriented BFO crystal [ $150\text{-}\mu\text{m}$ -thick  $(001)_{pc}$ , where pc denotes pseudocubic] studied in this work was grown in  $\text{Bi}_2\text{O}_3 + \text{B}_2\text{O}_3$  flux using a modified Kubel and Schmid growth [28]. The ferroelastic domain structure and lattice dynamics of the sample was previously investigated in detail by means of angle-dependent Raman spectroscopy, and the results were correlated with electron backscattered diffraction, polarized optical microscopy (POM), and piezoresponse force microscopy (PFM) [29]. In terms of domain size, the sample contains large macro (domain 1) and stripelike domains (domain 2) as shown in the POM image in Fig. 1(b). A detailed analysis showed that the stripelike domains have a  $71^\circ$  domain structure with an inclined DW, while macroscopic neighboring domains may have one of the four available DW variants or one of the eight degenerated electric polarization states [29,30].

BFO epitaxial thin film was grown by pulsed laser deposition on  $(110)$ -oriented orthorhombic  $\text{DyScO}_3$  (DSO) substrate. The growth parameters and detailed structure of the sample was analyzed by Talkenberger *et al.* [31]. In contrast to bulk single crystal, the PFM analysis performed shows two families of stripelike domains perpendicular to each other [Fig. 1(c)] with a stripe width of  $\sim 200$  nm.

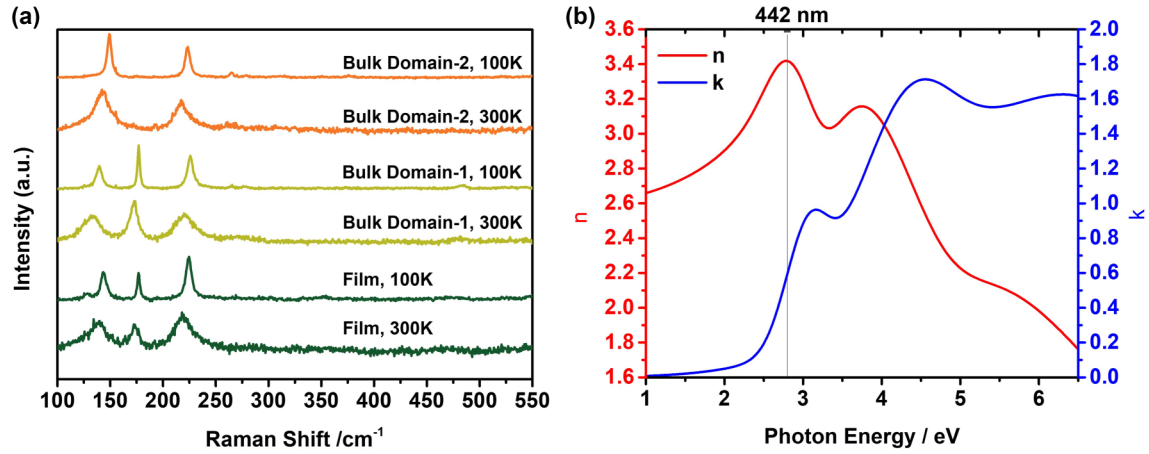


FIG. 2. (a) Raman spectra of BFO samples at 100 and 300 K. (b) Refractive index and extinction coefficient of the BFO thin-film sample.

The OTR technique was performed by using a Horiba LABRAM System-HR-800 (CCD camera, 2400 grooves per millimeter grating). The 442-nm line of a HeCd laser was used for excitation, the light being focused and collected through a 50-magnification objective with a numerical aperture of 0.5. For the accurate identification of peak positions, the spectra were first corrected using a calibration lamp and a Lorentzian peak fitting was performed. To obtain temperature-dependent spectra and thermal conductivity, a Linkam THMS-600 cooling-heating stage was used. The stage was continuously cooled by liquid-nitrogen vapor and operated between 100 and 350 K. A silver paste was applied to fix the sample to prevent sample drift and to provide a better thermal contact.

The OTR technique relies on the fact that the energy of Raman-active phonon modes is typically influenced by temperature. By harnessing this characteristic of Raman peaks, a calibration curve or a “thermometer” using the lowest possible laser power can be formed. The Raman spectra or the Raman peak centers obtained with a known higher excitation power contain quantitative information about the average local temperature rise ( $\Delta T$ ), which can be directly determined from the previously established calibration curve. The calculation of thermal conductivity becomes feasible through a model that considers a Gaussian laser beam, a semispherical heat transfer volume, and a known absorbed laser power when  $\Delta T$  is known [25,26,30].

Thermal conductivity was calculated based on a model derived for the local temperature rise due to the laser heating with the following formula [25]:

$$\kappa = \frac{\frac{\partial \omega}{\partial T}}{4\sqrt{\pi}d \frac{\partial \omega}{\partial P}}, \quad (1)$$

where  $\frac{\partial \omega}{\partial T}$  (cm<sup>-1</sup>/K) is the slope of the temperature calibration curve,  $\frac{\partial \omega}{\partial P}$  (cm<sup>-1</sup>/W) is the slope of the power-dependent Raman peak shift obtained at 150 and 300 K, and  $d$  is the laser spot size on the sample.

Well-defined peaks, such as those without any shoulders, with smaller full width at half maximum (FWHM), and high-intensity peaks, are a natural and preferred choice due to the

better peak fitting and sensitivity they provide. In the case of BFO, all three peaks (at 140, 170, and 220 cm<sup>-1</sup>) were well resolved (no shoulders), had nearly the same intensity, and exhibited similar FWHM. Thus, the thermal conductivity was calculated using all three peaks to prevent any bias in the results.

Spectroscopic ellipsometry was performed on the BFO/DSO sample using a M2000 J.A. Woollam ellipsometer at 55°, 60°, and 65° incidence angles in the 0.73–6 eV range. The data were evaluated to measure the thin-film sample thickness and the optical constants required for the thermal model, such as the refractive index, extinction coefficient, and absorption of the sample at the 442-nm laser line.

### III. RESULTS AND DISCUSSION

The Raman spectra of the bulk sample and thin film measured at 100 and 300 K are shown in Fig. 2(a). It is clear that all the observed peaks were broadened and shifted toward lower frequencies from 100 to 300 K as expected due to the thermal expansion and phonon anharmonicity [32]. The observed redshift is an important indicator of the applicability of the OTR method and is quantified in the next section. Peak assignments and peak intensity differences can be discussed based on the Raman tensor formalism considering the  $R3c$  (No. 161) space group of BFO. It predicts 27 optical phonon modes ( $\Gamma_{\text{opt}} = 4A_1 + 5A_2 + 9E$ ), 13 of which are Raman and IR active ( $A_1$  and double degenerate  $E$  modes) [29,33,34]. It has been reported that the macroscopic electric field of BFO splits the  $A_1$  and  $E$  Raman-active polar modes into longitudinal optical and transverse optical modes with different frequencies. Thus, observed Raman intensities become a complex function of the mixed symmetry character of the Raman tensor, crystal orientation, and ferroelastic polarization direction of the domains [29]. Based on the azimuthal angle Raman studies, the three Raman peaks observed at 140, 170, and 220 cm<sup>-1</sup> are thus assigned as  $E_{\text{TO}}-A_{1\text{TO}}$ ,  $A_{1\text{LO}}-E_{\text{LO}}$ , and  $A_{1\text{LO}}-A_{1\text{TO}}$ , respectively [29,31]. All three mixed symmetry peaks were observed for the bulk and thin-film samples, except for the 170-cm<sup>-1</sup> peak of the stripelike domain (domain-2) of the bulk sample. The absence of this peak is

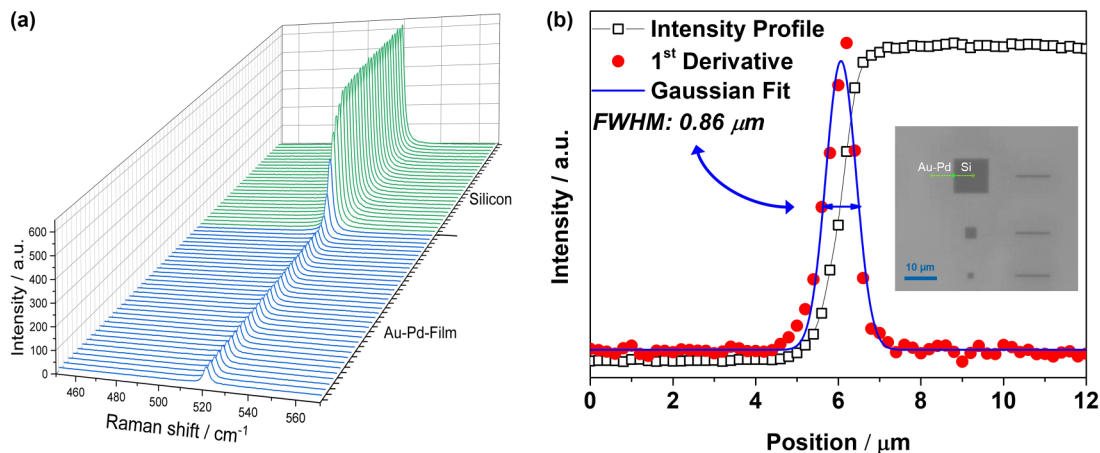


FIG. 3. (a) Raman line scan of the standard sample. (b) Intensity profile and Gaussian fit to first derivative of the intensity profile. FWHM (spot size) is shown with a blue arrow on the fitted Gaussian line.

due to the orientational dependence of the Raman modes as explained. On the other hand, the good signal-to-noise ratio and the clear temperature-dependent redshift indicate that all observed peaks can be used in temperature calibration (or as a thermometer) for the OTR method.

To obtain accurate  $\frac{\partial\omega}{\partial P}$  ( $\text{cm}^{-1}/\text{W}$ ) values, it is necessary to know how much of the laser power is absorbed by the sample. Therefore, ellipsometry measurement was performed and the refractive index and extinction coefficient dispersion curves are shown in Fig. 2(b). For the 442-nm laser line ( $\sim 2.80$  eV) a refractive index and extinction coefficient of 3.42 and 0.61 was found, respectively. These values are used to calculate the penetration depth [ $\delta(\lambda) = \lambda/4\pi k$ ] and the percentage of laser absorption by the sample using a modified Fresnel equation where transmission is considered zero:

$$\alpha = 1 - \frac{(n-1)^2 + k^2}{(n+1)^2 + k^2}. \quad (2)$$

It has been found that BFO absorbs  $\sim 69\%$  of the 442 nm of the laser line. Moreover, the laser penetrates  $\sim 60$  nm below the surface, which is three times smaller than the thickness of the thin film (180 nm). This explains why there is no DSO (substrate) Raman peak observed for the thin-film sample. Therefore, the BFO/DSO interface should have a negligible effect on the laser heated volume. Moreover, in the case of single crystal, laser penetration into another domain may impact the results, particularly due to domain wall scattering. Our previous depth profile study on the stripelike domains has shown that the minimum thickness of the domains is larger than  $7 \mu\text{m}$  [29], which is a sufficiently large value compared to the 60-nm penetration depth. This improves the reliability of the bulk OTR model used in this work.

Laser spot size is another important parameter in the OTR model and was measured directly using a 20-nm Au-Pd coated Si calibration standard using a similar procedure reported in literature [35]. A Raman line scan with a 200-nm step size was performed to record the Si peak intensity [Fig. 3(a)] from the Au-Pd coated and etched Si area of  $10 \times 10 \mu\text{m}^2$  shown in the inset of Fig. 3(b). The intensity profile of the scanned line, the first derivative of the intensity, and the Gaussian fit

are shown in Fig. 3(b). The FWHM of the Gaussian fit gives a spot size of 860 nm, larger than the Abbe's diffraction-limited spot size ( $0.51\lambda / \text{NA}$ ) due to several factors such as optical and chromatic aberrations, instrument setup, and focusing distance effecting broadening of the beam.

The temperature calibration data from 100 to 350 K for the  $A_{1\text{LO}}-A_{1\text{TO}}$  mode [Fig. 4(a)] and the laser power-dependent peak shift at room temperature and 150 K [Figs. 4(b) and 4(c)] are shown in Fig. 4. A linear temperature and laser power dependence was found for both single-crystal and thin-film samples. Therefore, their slopes can be used to calculate the thermal conductivity using Eq. (1). In addition to the linear temperature and power dependence, a clear shift between the peak centers of domain 1 and domain 2 of the bulk sample was recorded for both temperature- and power-dependent data. The shift is attributed to the angular dispersion of oblique phonon modes, as described by Hlinka *et al.*, and variations in domain polarization orientations relative to each other [36]. However, the slopes of the calibration ( $\frac{\partial\omega}{\partial T}$ ) and the power-dependent lines ( $\frac{\partial\omega}{\partial P}$ ) of domain 1 and domain 2 are almost similar (see Table I), indicating the same or close thermal conductivity for different domains of the bulk sample.

The slopes of all remaining peaks and the thermal conductivity values derived from Eq. (1) are shown in Table I. The data are plotted in Fig. 5 and compared with available references. Comparing the thermal conductivity of single crystals with bulk using literature data is challenging due to the sensitivity of thermal conductivity to factors such as porosity, grain size, doping levels, and defects. For instance, at 300 K, for nanocrystalline BFO with a grain size of 100-nm, values ranging from 0.19 to 0.38 W/mK have been reported [37], with the low thermal conductivity attributed to the porosity of the pellets. In contrast, polycrystalline BFO at 300 K exhibits a thermal conductivity of 3.5 W/mK, and the introduction of Ca and Ba doping significantly reduces thermal conductivity to 2 W/mK due to point defect scattering [38]. Furthermore, Khasbulatov *et al.* found similar thermal conductivity for an undoped sample (3.5 W/mK) and significant reduction for rare-earth doped samples [39]. Additionally, another sintered BFO product has been reported to possess a thermal

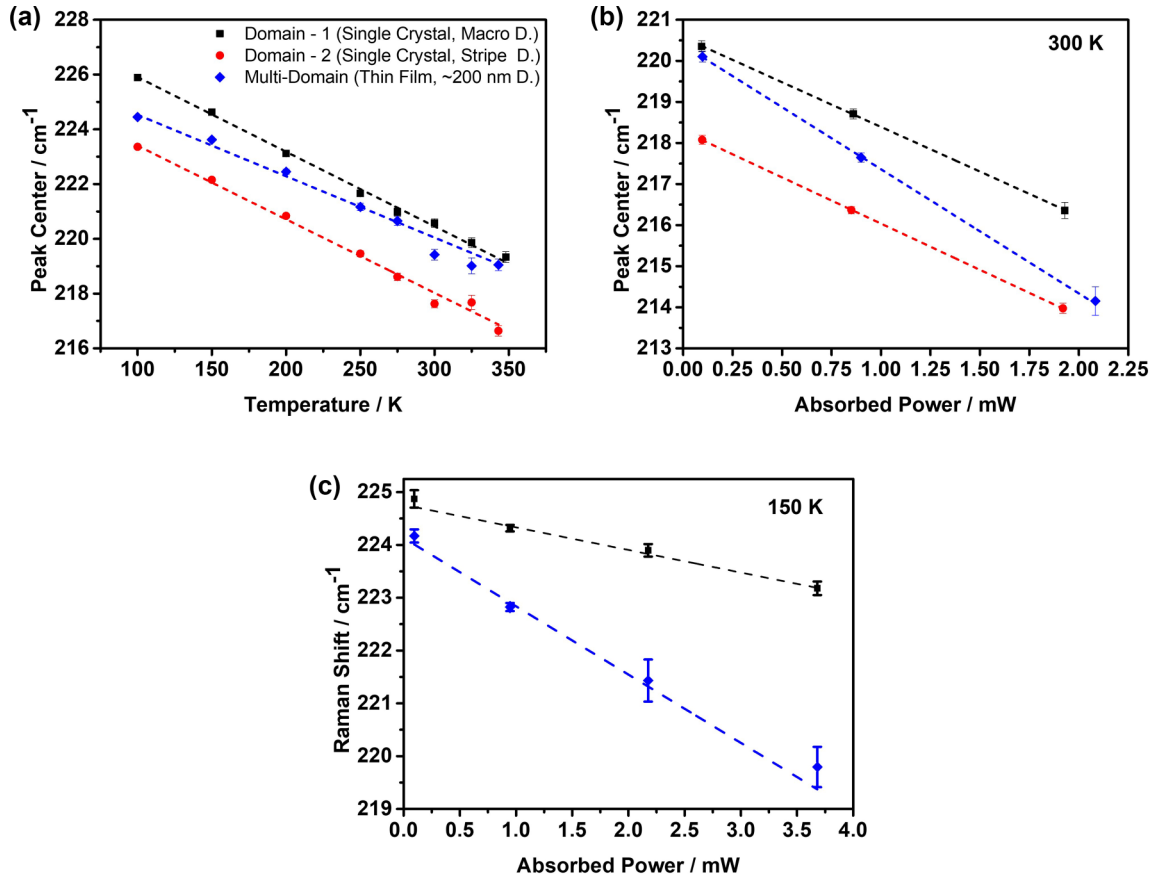


FIG. 4. (a) Temperature-dependent peak shift (calibration line). (b) Laser power-dependent peak shift at room temperature and (c) 150 K. Note that D. refers to domain.

conductivity of 0.8 W/mK [40]. In this context, the bulk thermal conductivity values of single crystals reported in the paper fall within the range of 0.8–3.5 W/mK, which aligns closely with the existing bulk literature data. In addition to room temperature measurements, at 150 K, the bulk sample exhibits a thermal conductivity of  $9.89 \pm 0.84$  W/mK, which is approximately 50% higher than the low-temperature value

reported by Ramachandran *et al.* [38]. This disparity can be attributed to the single-crystal nature of our sample, in contrast to the polycrystalline nature of the sintered sample mentioned in the study [38], where phonon grain boundary scattering plays an additional role in reducing thermal conductivity.

The domain 1 ( $1.96 \pm 0.33$  W/mK) and domain 2 ( $2.17 \pm 0.50$  W/mK) values of single-crystal BFO are in good

TABLE I. Temperature and power slopes and corresponding thermal conductivities of three BFO Raman-active modes for single-crystal and thin-film samples for 300 and 150 K.

Sample	Temperature slope (cm <sup>-1</sup> /K)	Power slope (cm <sup>-1</sup> /W) (300 K)	Power slope (cm <sup>-1</sup> /W) (150 K)	Thermal conductivity (W/mK) (300 K)	Thermal conductivity (W/mK) (150 K)
Single crystal Domain 1				$1.96 \pm 0.33$	$9.89 \pm 0.84$
$E_{TO}-A_{1TO}$	$-35.1 \times 10^{-3} \pm 9 \times 10^{-4}$	$-3059 \pm 330$	$-523 \pm 67$	$2.18 \pm 0.40$	$10.39 \pm 1.25$
$A_{1LO}-E_{LO}$	$-22.7 \times 10^{-3} \pm 7 \times 10^{-4}$	$-2229 \pm 224$	$-350 \pm 22$	$1.67 \pm 0.18$	$9.95 \pm 0.64$
$A_{1LO}-A_{1TO}$	$-26.8 \times 10^{-3} \pm 6 \times 10^{-4}$	$-2162 \pm 230$	$-440 \pm 31$	$2.04 \pm 0.22$	$9.36 \pm 0.64$
Single crystal Domain 2				$2.17 \pm 0.50$	
$E_{TO}-A_{1TO}$	$-34.7 \times 10^{-3} \pm 7 \times 10^{-4}$	$-3122 \pm 478$	$-1842 \pm 369$	$1.84 \pm 0.27$	
$A_{1LO}-A_{1TO}$	$-27.5 \times 10^{-3} \pm 1 \times 10^{-4}$	$-1842 \pm 369$		$2.45 \pm 0.48$	
Thin film				$1.16 \pm 0.12$	$3.20 \pm 0.40$
$E_{TO}-A_{1TO}$	$-33.4 \times 10^{-3} \pm 2 \times 10^{-4}$	$-4401 \pm 495$	$-1689 \pm 197$	$1.37 \pm 0.15$	$3.06 \pm 0.37$
$A_{1LO}-E_{LO}$	$-17.7 \times 10^{-3} \pm 1 \times 10^{-4}$	$-2525 \pm 331$	$-843 \pm 128$	$1.00 \pm 0.16$	$3.26 \pm 0.51$
$A_{1LO}-A_{1TO}$	$-24.2 \times 10^{-3} \pm 1 \times 10^{-4}$	$-3255 \pm 515$	$-1133 \pm 109$	$1.12 \pm 0.07$	$3.29 \pm 0.33$

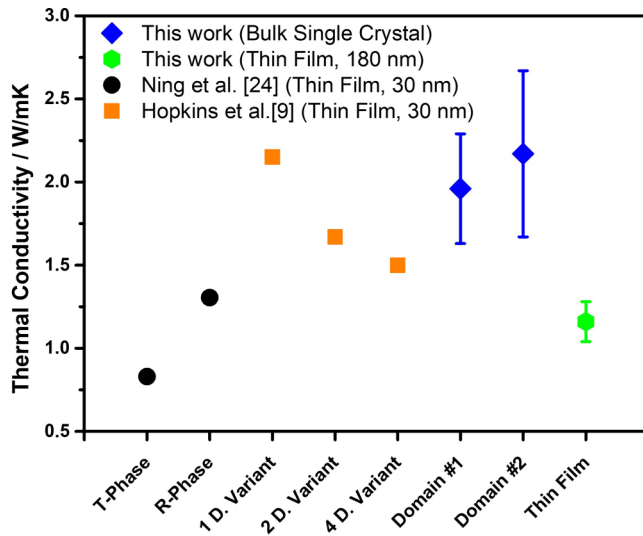


FIG. 5. Thermal conductivity of BFO samples studied in this work (BFO single-crystal and multidomain 180-nm-thick, thin film) at 300 K together with relevant reference studies.

agreement with each other. Furthermore, these values are in excellent agreement with epitaxially grown single-domain thin films (30 nm) of BFO reported by Hopkins *et al.* ( $\sim 2.15$  W/mK) [9]. This result indicates that the ferroelastic polarization direction of the domains has no significant effect on the heat transport and a saturation in the thermal conductivity value can be expected for single-domain variants of BFO. On the other hand, the thermal conductivity of the thin-film sample (1.16 W/mK) was found to be  $\sim 46\%$  smaller than that of the single-domain variants of the bulk sample at room temperature. Considering the very high spot size (860 nm) to penetration depth ratio (60 nm) of the laser, a radial heat flow would encounter several domain walls when a  $\sim 200$ -nm domain width [Fig. 1(c)] is considered. Thus, this suggests that the origin of the reduced thermal conductivity comes from the thermal boundary resistance of DWs. In fact, this OTR thermal conductivity once again corroborates well with the four-variant ( $\sim 1.50$  W/mK; Hopkins *et al.* [9]) and multidomain R-like thin films (1.29–1.32 W/mK; Ning *et al.* [24]). Together with the seminal studies reported by Ning *et al.* and

Hopkins *et al.* it can be concluded that the thermal conductivity of multiferroic BFO is strongly affected by the density of the domain walls. Furthermore, at 150 K, it is observed that the thermal conductivity of both the bulk sample ( $9.89 \pm 0.84$  W/mK) and the thin-film sample ( $3.20 \pm 0.40$  W/mK) is higher than at room temperature, as expected. Notably, the thermal conductivity of the bulk sample increases by a factor of approximately 5 from room temperature to 150 K, while the thin-film sample shows a more modest increase of about 2.8 times. This observation is consistent with the idea of domain wall scattering, which may potentially limit the increase in thermal conductivity in multidomain samples at low temperatures.

Therefore, domain wall density engineering with an external electric or strain field could potentially provide 46% bidirectional thermal conductivity control for the BFO at room temperature.

#### IV. CONCLUSION

We have determined the thermal conductivity of BiFeO<sub>3</sub> ferroelastic domains in both bulk and thin film using temperature-dependent Raman measurements combined with excitation power sensitive measurement. A thermal conductivity model that assumes strong surface absorption of the Gaussian beam and heat conduction into a semi-infinite half space is used. It was found that the differences in the values of thermal conductivity obtained for bulk and thin films can be discussed in terms of the influence of the ferroelastic domain walls. DWs were found to act as effective phonon scatterers, reducing the thermal conductivity at room temperature from 2.17 to 1.16 W/mK, and from 9.89 to 3.20 W/mK at 150 K. Such a thermal conductivity difference between single-domain and multi-BFO hints toward strong phonon domain wall scattering or thermal boundary resistance of domain walls.

#### ACKNOWLEDGMENTS

This work was performed within the Deutsche Forschungsgemeinschaft (DFG) Project No. 441856638. The authors thank Ionela Lindfors-Vrejoiu and Florian Johann for the thin-film samples and PFM measurements.

- [1] A. L. Moore and L. Shi, *Mater. Today* **17**, 163 (2014).
- [2] N. Li, J. Ren, L. Wang, G. Zhang, P. Hänggi, and B. Li, *Rev. Mod. Phys.* **84**, 1045 (2012).
- [3] Z. Chen, X. Zhang, and Y. Pei, *Adv. Mater.* **30**, 1705617 (2018).
- [4] E. S. Toberer, L. L. Baranowski, and C. Dames, *Annu. Rev. Mater. Res.* **42**, 179 (2012).
- [5] J. Chen, X. Xu, J. Zhou, and B. Li, *Rev. Mod. Phys.* **94**, 025002 (2022).
- [6] M. Hamid Elsheikh, D. A. Shnawah, M. F. M. Sabri, S. B. M. Said, M. Haji Hassan, M. B. Ali Bashir, and M. Mohamad, *Renew. Sustain. Energy Rev.* **30**, 337 (2014).
- [7] M. Royo, C. Escorihuela-Sayalero, J. Íñiguez, and R. Rurali, *Phys. Rev. Mater.* **1**, 051402(R) (2017).
- [8] S. Li, X. Ding, J. Ren, X. Moya, J. Li, J. Sun, and E. K. H. Salje, *Sci. Rep.* **4**, 6375 (2014).
- [9] P. E. Hopkins, C. Adamo, L. Ye, B. D. Huey, S. R. Lee, D. G. Schlom, and J. F. Ihlefeld, *Appl. Phys. Lett.* **102**, 121903 (2013).
- [10] X. Ding and E. K. H. Salje, *AIP Adv.* **5**, 053604 (2015).
- [11] J. A. Seijas-Bellido, C. Escorihuela-Sayalero, M. Royo, M. P. Ljungberg, J. C. Wojdel, J. Íñiguez, and R. Rurali, *Phys. Rev. B* **96**, 140101(R) (2017).
- [12] A. J. H. Mante and J. Volger, *Physica* **52**, 577 (1971).
- [13] M. A. Weilert, M. E. Msall, A. C. Anderson, and J. P. Wolfe, *Phys. Rev. Lett.* **71**, 735 (1993).
- [14] J. F. Ihlefeld, B. M. Foley, D. A. Scrymgeour, J. R. Michael, B. B. McKenzie, D. L. Medlin, M. Wallace, S. Trolier-Mckinstry, and P. E. Hopkins, *Nano Lett.* **15**, 1791 (2015).
- [15] B. M. Foley, M. Wallace, J. T. Gaskins, E. A. Paisley, R. L. Johnson-Wilke, J. W. Kim, P. J. Ryan, S. Trolier-Mckinstry,

- P. E. Hopkins, and J. F. Ihlefeld, *ACS Appl. Mater. Interfaces* **10**, 25493 (2018).
- [16] E. Langenberg, D. Saha, M. E. Holtz, J.-J. Wang, D. Bugallo, E. Ferreira-Vila, H. Paik, I. Hanke, S. Ganschow, D. A. Muller, L.-Q. Chen, G. Catalan, N. Domingo, J. Malen, D. G. Schlom, and F. Rivadulla, *Nano Lett.* **19**, 7901 (2019).
- [17] A. J. Preethi and M. Ragam, *J. Adv. Dielectr.* **11**, 2130001 (2021).
- [18] T. Choi, S. Lee, Y. J. Choi, V. Kiryukhin, and S.-W. Cheong, *Science* **324**, 63 (2009).
- [19] R. Ramesh and N. A. Spaldin, *Nanosci. Technol.* **3**, 20 (2009).
- [20] Y. Liu, Y. Wang, J. Ma, S. Li, H. Pan, C.-W. Nan, and Y.-H. Lin, *Prog. Mater. Sci.* **127**, 100943 (2022).
- [21] R. J. Zeches, M. D. Rossell, J. X. Zhang, A. J. Hatt, Q. He, C.-H. Yang, A. Kumar, C. H. Wang, A. Melville, and C. Adamo, *Science* **326**, 977 (2009).
- [22] G. Catalan and J. F. Scott, *Adv. Mater.* **21**, 2463 (2009).
- [23] G. Chen, J. Chen, W. Pei, Y. Lu, Q. Zhang, Q. Zhang, and Y. He, *Mater. Res. Bull.* **110**, 39 (2019).
- [24] S. Ning, S. C. Huberman, C. Zhang, Z. Zhang, G. Chen, and C. A. Ross, *Phys. Rev. Appl.* **8**, 054049 (2017).
- [25] B. Stoib, S. Filser, J. Stötzel, A. Greppmair, N. Petermann, H. Wiggers, G. Schierning, M. Stutzmann, and M. S. Brandt, *Semicond. Sci. Technol.* **29**, 124005 (2014).
- [26] T. Beechem, L. Yates, and S. Graham, *Rev. Sci. Instrum.* **86**, 041101 (2015).
- [27] J. Jaramillo-Fernandez, E. Chavez-Angel, and C. M. Sotomayor-Torres, *Appl. Therm. Eng.* **130**, 1175 (2018).
- [28] F. Kubel and H. Schmid, *J. Cryst. Growth* **129**, 515 (1993).
- [29] C. Himcinschi, J. Rix, C. Röder, M. Rudolph, M. M. Yang, D. Rafaja, J. Kortus, and M. Alexe, *Sci. Rep.* **9**, 379 (2019).
- [30] F. Zavaliche, R. R. Das, D. M. Kim, C. B. Eom, S. Y. Yang, P. Shafer, and R. Ramesh, *Appl. Phys. Lett.* **87**, 182912 (2005).
- [31] A. Talkenberger, I. Vrejoiu, F. Johann, C. Röder, G. Irmer, D. Rafaja, G. Schreiber, J. Kortus, and C. Himcinschi, *J. Raman Spectrosc.* **46**, 1245 (2015).
- [32] M. Balkanski, R. F. Wallis, and E. Haro, *Phys. Rev. B* **28**, 1928 (1983).
- [33] R. Haumont, J. Kreisel, and P. Bouvier, *Phase Transitions* **79**, 1043 (2006).
- [34] M. K. Singh, H. M. Jang, S. Ryu, and M. H. Jo, *Appl. Phys. Lett.* **88**, 042907 (2006).
- [35] E. Bayati, A. Zhan, S. Colburn, M. V. Zhelyeznyakov, and A. Majumdar, *Appl. Opt.* **58**, 1460 (2019).
- [36] J. Hlinka, J. Pokorny, S. Karimi, and I. M. Reaney, *Phys. Rev. B* **83**, 020101(R) (2011).
- [37] M. R. Islam, M. A. Zubair, R. H. Galib, M. S. Bin Hoque, J. A. Tomko, K. Aryana, A. K. Basak, and P. E. Hopkins, *ACS Appl. Mater. Interfaces* **14**, 25886 (2022).
- [38] B. Ramachandran, K. K. Wu, Y. K. Kuo, and M. S. Ramachandra Rao, *J. Phys. D.: Appl. Phys.* **48**, 115301 (2015).
- [39] S. Khasbulatov, S. Kallaev, H. Gadjiev, Z. Omarov, A. Bakmaev, I. Verbenko, A. Pavelko, and L. Reznichenko, *J. Adv. Dielectr.* **10**, 2060019 (2020).
- [40] A. I. Klyndyuk and A. A. Khort, *High Temp.* **57**, 186 (2019).